Bio-reductive hetero-bimetallic Co(III)-Pt(II) complex for tumor-selective platinum release and cytotoxicity

Sharmila Wahengbam,[a] Neha Masarkar,[b] Himanshi Sharma,[c] Sukhes Mukherjee,[b] Chandi C. Malakar,[a] Mithun Roy[d]*

[a.] *Department of Chemistry, National Institute of Technology Manipur*
Langol, Imphal West - 795004
E-mail: mithunroy@nitmanipur.ac.in, mithunroy.iisc@gmail.com
[b.] *Department of Biochemistry, All India Institute of Medical Sciences, Bhopal*
Saket Nagar, Bhopal, Madhya Pradesh – 462020
E-mail: sukhes.biochemistry@aiimsbhopal.edu.in
[c.] *Kusuma School of Biological Sciences, Indian Institute of Technology Delhi*
Hauz Khas, New Delhi – 110016
[d] *Department of Chemistry, National Institute of Technology Agartala*
Jirania-799046, West Tripura, Tripura (INDIA)

Supporting Information

Methods

BSA Binding

BSA (Bovine Serum Albumin) transports administered drugs into the bloodstream to the target site. Therefore, it is necessary to identify the ability of the complex to bind with BSA as a model for human serum albumin. The binding ability was assessed using a photoluminescence emission at 339 nm (λ_{ex}=280 nm) in HITACHI F-7000 fluorescence spectrophotometer at 298K. The emission property of BSA comes from the presence of tryptophan, tyrosine, and phenylalanine residue. The gradual addition of complexes (1 mM) to a solution of BSA (3 X 10^{-5} M) in 10 mM Tris-HCl buffer 7.2 pH significantly quenched the emission intensity of BSA. The binding constant of the two complexes was determined using the Stern-Volmer equation and the Scatchard plot.

$$\frac{I_0}{I} = 1 + K_{sv}[Q] = 1 + K_q\tau_0[Q]$$

Where I is the fluorescence intensity of BSA, I_0 is the fluorescence intensity after adding complex to BSA, K_{sv} is the Stern-Volmer quenching constant, [Q] is the concentration of complex, K_q is the rate constant and $\boldsymbol{\tau}_o$ is the average lifetime.[S1]

Molecular Docking Studies.

The molecular geometry optimization of complex **[Co(III)-Pt(II)]** was carried out using Gaussian 09 DFT methods with B3LYP functional and basic set 6-31+G(d,p) for H,C,N,O and Cl atoms, LANL2DZ for Cobalt atom and SDD for Platinum atom. The crystal structure of BSA was obtained from Protein Data Bank (PDB ID: 3v03) at a resolution of 2.70 Å. Docking calculations were performed by using AutoDock 1.5.6 using Lamarckian genetic algorithm (LGA). Discovery studio was used to produce molecular images. The three dimensional (x,y,z) grid box was set at 126 Å x 78 Å x 98 Å with spacing 0.375 Å to focus all binding site in the BSA. Polar hydrogens were added and Kollman charges were calculated.

Electrochemical analysis

Electrochemical properties of **[Co(III)(L^1)(phen-NH_2)](acac)$_3$**, **[Pt(II)(DABA)Cl_2]** and **[Co(III)-Pt(II)](acac)$_3$** were analyzed using cyclic 5haracteriz studies carried out in DMF using glassy carbon as the working electrode, Ag/AgCl and Hg/Hg_2Cl_2 as the reference electrode, Pt as the counter electrode, and KCl (0.1 M) as the supporting electrode at a scan rate of 50 mV/s. Anodic and cathodic scan of **[Co(III)-Pt(II)](acac)$_3$** in the presence of an increasing volume of Glutathione (10 μM) shows the reduction of Co(III) centre to Co(II) in the cathodic scan and oxidation of GSH to GSSG in the anodic scan.

Scan Rate–Dependent Cyclic Voltammetry and Graph Fitting

Cyclic voltammograms were recorded at different scan rates to evaluate the electron-transfer characteristics of the complex.

Ip vs. $\nu^{1/2}$ plot – A linear fit was applied to examine diffusion-controlled behavior as predicted by the Randles–Sevcik equation.

$$Ip = (2.69\times10^5)\, n^{3/2} A C D^{1/2} \nu^{1/2}$$

where *n* is the number of electrons transferred, *A* the electrode area (cm^2), *C* the analyte concentration (mol cm^{-3}), and *D* the diffusion coefficient (cm^2s^{-1}). [S2] A linear Ip vs. $\nu^{1/2}$ relationship confirms diffusion control.

Cell lineages

MDA-MB-231 (human breast adenocarcinoma), HT-29 (human colon adenocarcinoma) cells were maintained in Dulbecco's Modified Eagle Medium (DMEM). A549 (human lung carcinoma) and HaCaT (human immortalized keratinocytes) were cultured in DMEM/F12 with 10% FCS. All cell lines were maintained in the presence of 1x antibiotic-antimycotic solution purchased from Thermo Fisher Scientific. All the cell lines were maintained at 37 ^{0}C with 5% CO_2.

Cytotoxicity Assay

Cell viability was measured in triplicates in 96-well plates with a cell density of 6000-8000 cells per well using MTT [3-(4,5-dimethylthiazol-2-yl)-2,5-diphenyltetrazo-lium bromide]. All the cells were incubated for 24 h in normoxia (5% CO_2, 95% atmospheric air at 37 ^{0}C) conditions, and to mimic hypoxia, A459 cell were incubated with 100 µM $CoCl_2$ as described previously.[S3] The cells were treated with complexes for 24 h in triplicate and after the treatment, the cells were further incubated with 10 µL MTT solution (5mg/ml in 1X PBS) for 3 h at 37 ^{0}C. Formazan crystals were dissolved in 100 µL DMSO and the absorbance was taken in 570 nm using Cytation 5, BioTek with 690 nm as reference. The graphs were plotted using GraphPad Prism 7 software.

Scratch Wound Healing assay

MDA-MB 231 cells were seeded in a 6-well plate and incubated in 2 mL of complete DMEM media at 37 ^{0}C and 5% CO_2 till the monolayer achieved 70% confluency. The complete media was then replaced by serum-free media. Using a sterile 10 µl pipette tip, a straight scratch was made simulating a wound in each of the wells. The plate was then washed with 1 ml of 1X PBS buffer to remove debris and then replaced with 2 ml of serum-free media. The **[Co(III)-Pt(II)](acac)$_3$** compounds at IC_{50} concentrations were added and images were taken at 0, 24 hr following the treatment from at least 3 different fields of each well. The width of the wound was measured and the % of wound healing was calculated.

Cellular Uptake Study- Inductively coupled plasma mass spectrometry (ICP-MS)

Inductively coupled plasma mass spectrometry (ICP-MS) (for trace elemental analysis) was carried out to determine the concentration of Cobalt (^{59}Co) and Platinum (^{195}Pt) in [Co(III)-Pt(II)] treated cell pellet. Briefly 3x10^5 cells were seeded in 60 mm cell culture dish and incubated overnight at 37^{0}C. Next day, cells were treated with 10 µM of **[Co(III)-Pt(II)](acac)$_3$** (5%-DMSO-milliQ stock) and incubated for predetermined time points (3 h, 6 h, 12 h, and 24 h). After incubation, cells were washed with 1X PBS, and then trypsinized and collected. The cell number was counted by hemocytometer. Finally, the cells were digested with 1mL of 70% HNO_3 solution and the total volume was made up to 12 mL by milliQ, followed by ICP-MS analysis using Agilent 7850 ICP-MS instrument.

Real-Time Revere Transcription-Polymerase chain reaction (RT-PCR)

1. RNA isolation: To induce cellular physiological hypoxia, the incubator chamber was maintained at an oxygen level of 1% to achieve hypoxia. MDA-MB 231 cells were seeded in a 6-well plate and incubated in 2 ml of complete DMEM media at 37 °C and 5% CO_2 till the monolayer achieved 70 – 80 % confluency. Later the cells were treated with **[Co(III)-Pt(II)](acac)$_3$** at IC_{50} concentration for 24 hours. Total RNA was isolated from a single-cell suspension of cultured

cells using the Trizol method. RNA concentration and purity were measured using a NanoDrop Spectrophotometer.

For all experiments performed in hypoxia around 50-100 μM of Cobalt chloride was added as it stabilizes the HIF expression.

2. Reverse-transcription: The cDNA synthesis was carried out using 1 μg RNA using the RevertAid First Strand cDNA Synthesis Kit (Thermo Scientific) following the manufacturer's protocol.

3. Real-time polymerase chain reaction (PCR): The real-time polymerase chain reaction (PCR) was carried out using gene-specific primers for HIF-1α, VEGF, and GLUT1 via SYBR green method following manufacturer's protocol. Primer sequences are available on request.

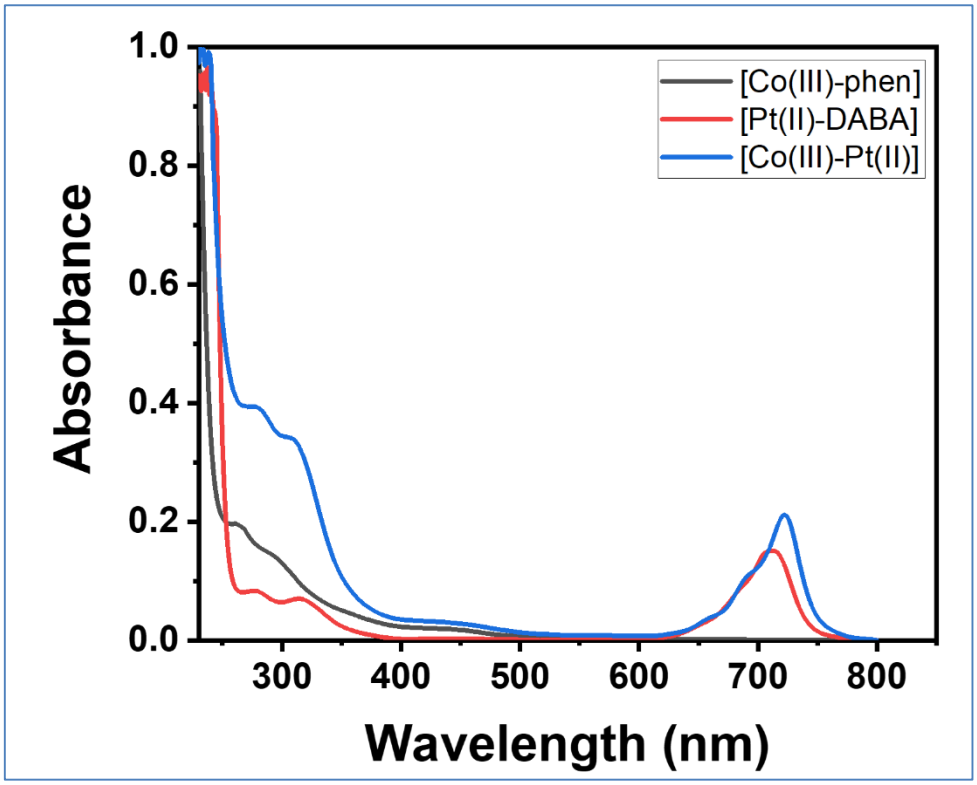

Figure S1. Normalized UV-Vis spectra of **[Co(III)(L^1)(phen-NH$_2$)](acac)$_3$**, **[Pt(II)(DABA)Cl$_2$]** and **[Co(III)-Pt(II)](acac)$_3$** complex, **([Co(III)-Pt(II)])** (1.0 mmol.L^{-1})

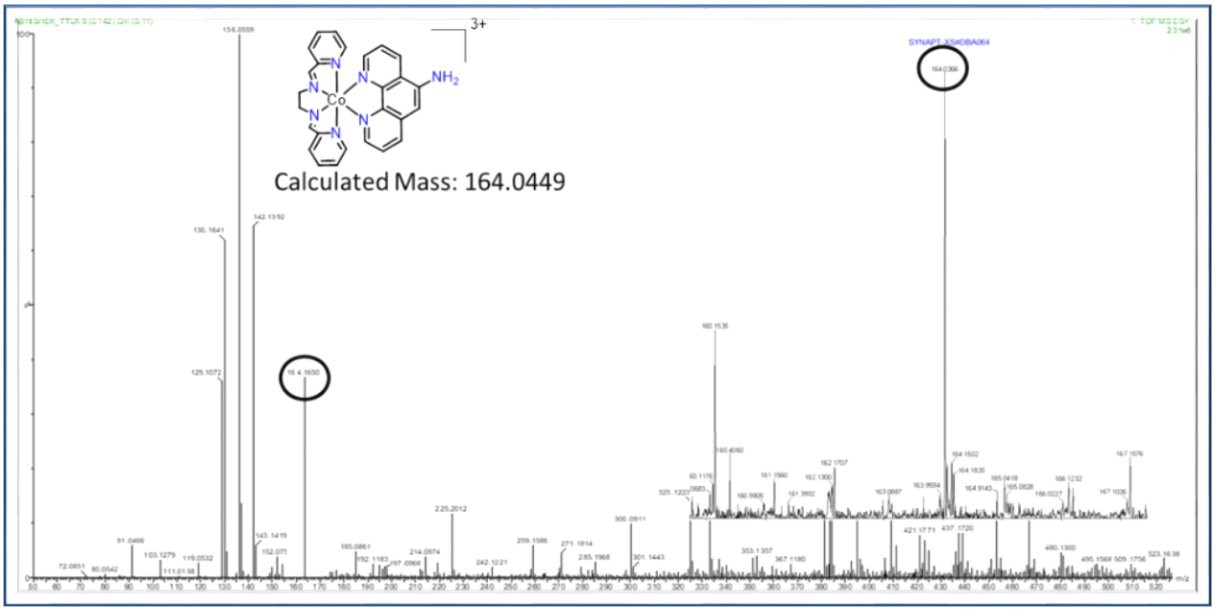

Figure S2. Q-TOF ESI Mass spectra of **[Co(III)(L^1)(phen-NH$_2$)](acac)$_3$** recorded in CH_3OH using Waters Micromass Q-Tof Micro spectro-photometer. The peak at m/z 164.1650 corresponds to the species $[M]^{3+.}$ The inset shows the isotropic distribution of the peak at 164.0366 of **[Co(III)(L^1)(phen-NH$_2$)](acac)$_3$**

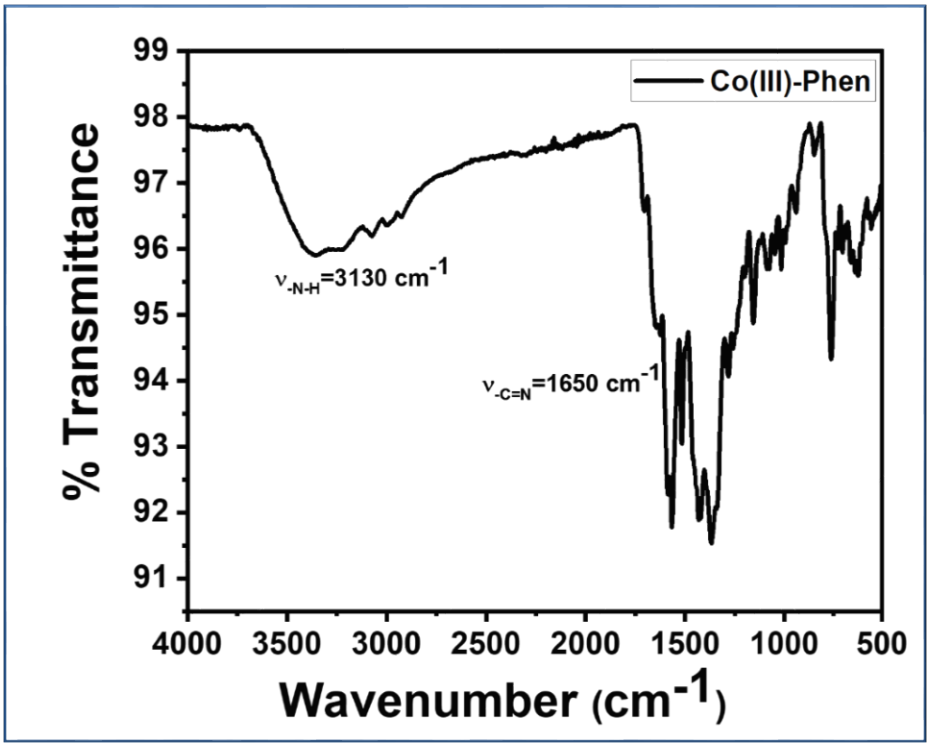

Figure S3. FT-IR Spectra of **[Co(III)(L^1)(phen-NH_2)](acac)$_3$** with characteristic peaks at 1650 cm^{-1} and 3130 cm^{-1} representing imine bond and amine bond recorded using Perkin-Elmer UATR TWO FT-IR Spectrometer

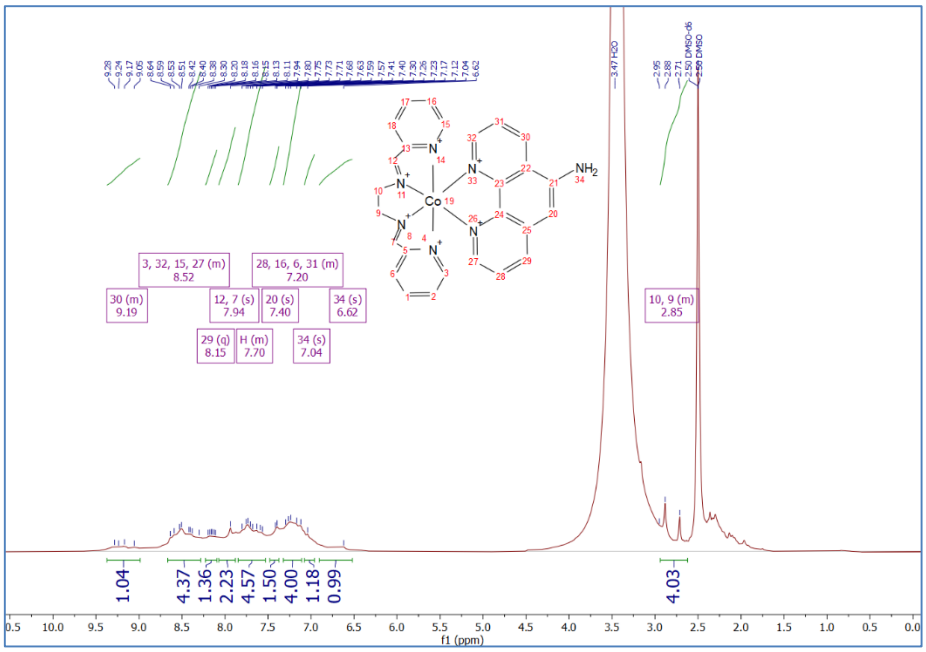

Figure S4. ^{1}H NMR spectra of **[Co(III)(L^1)(phen-NH_2)](acac)$_3$** recorded in DMSO-d_6 using Bruker Avance 400 (400 MHz). The peaks in the aromatic region (δ 9.3–7.2 ppm) arise from both the phenanthroline and Schiff base aromatic environments. The singlets at δ 7.04 and 6.62 ppm correspond to the amine protons. The peak in the range δ 2.96-2.67 ppm arises from methyl protons of the ancillary ligand, and the singlet at δ 7.94 ppm is attributed to the imine-adjacent aromatic proton (–CH=N–Ar).

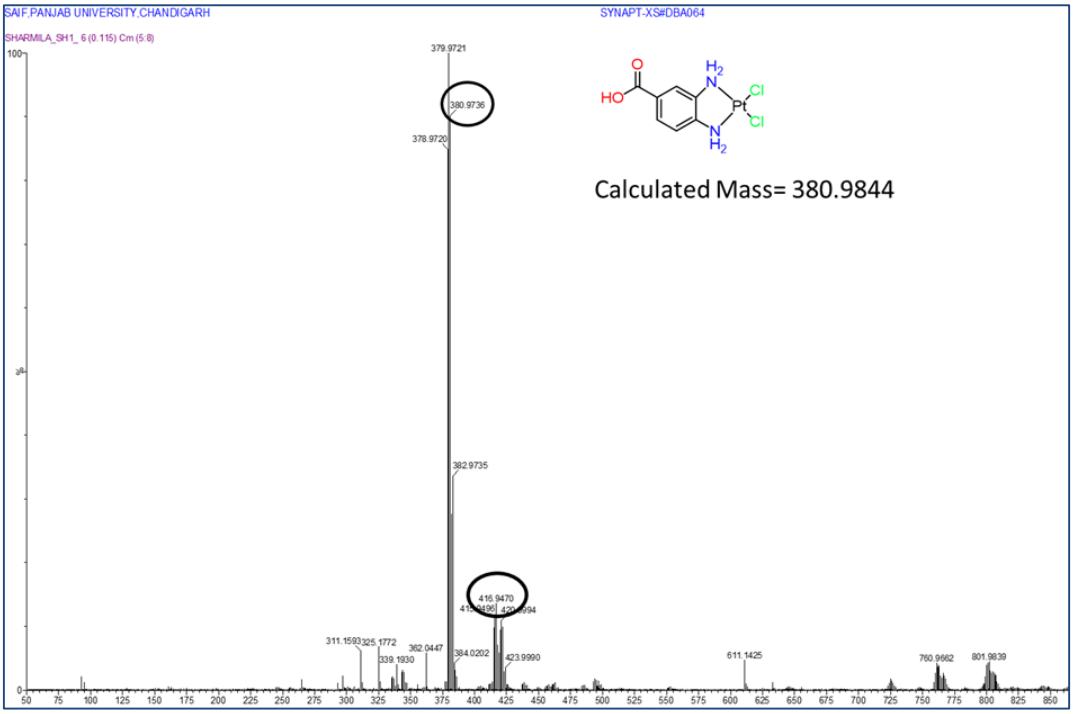

Figure S5. Q-TOF ESI Mass spectra of **[Pt(II)(DABA)Cl$_2$]** recorded in CH_3OH using Waters Micromass Q-Tof Micro spectro-photometer. The peak at m/z 380.9736 corresponds to the species $[M\text{-}Cl\text{-}H]^+$ and 416.9470 correspond to $[M]^+$ of complex **[Pt(II)(DABA)Cl$_2$]**

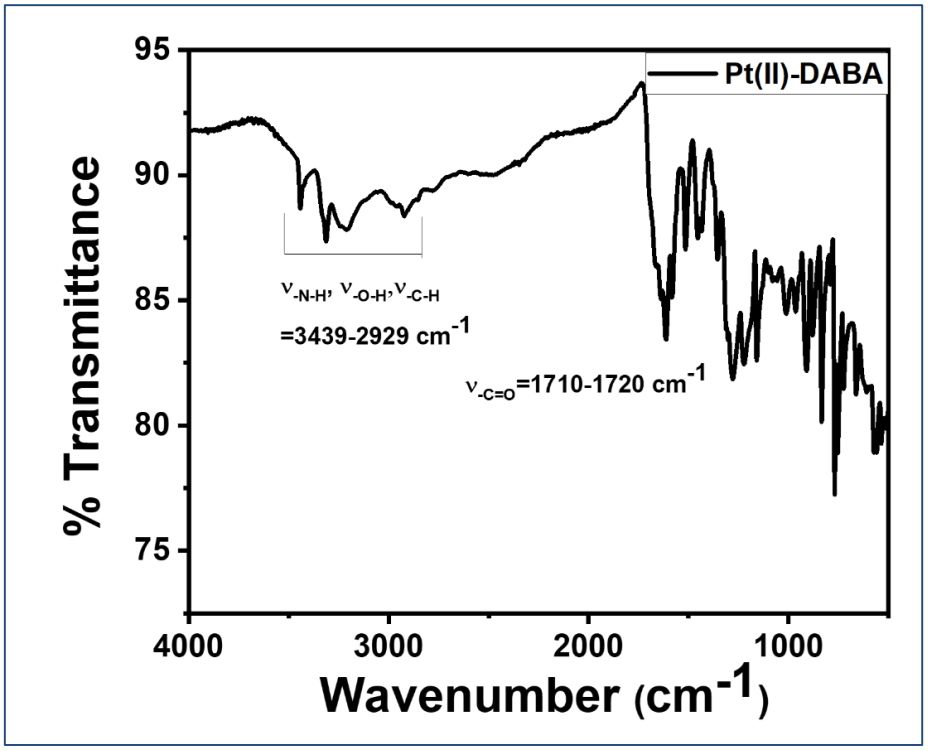

Figure S6. FT-IR Spectra of **[Pt(II)(DABA)Cl$_2$]** with characteristic peaks at 1710-1720 cm^{-1} and 3439-2929 cm^{-1} representing carbonyl bond, amine bond, and hydroxyl (O-H) bond recorded using Perkin-Elmer UATR TWO FT-IR Spectrometer

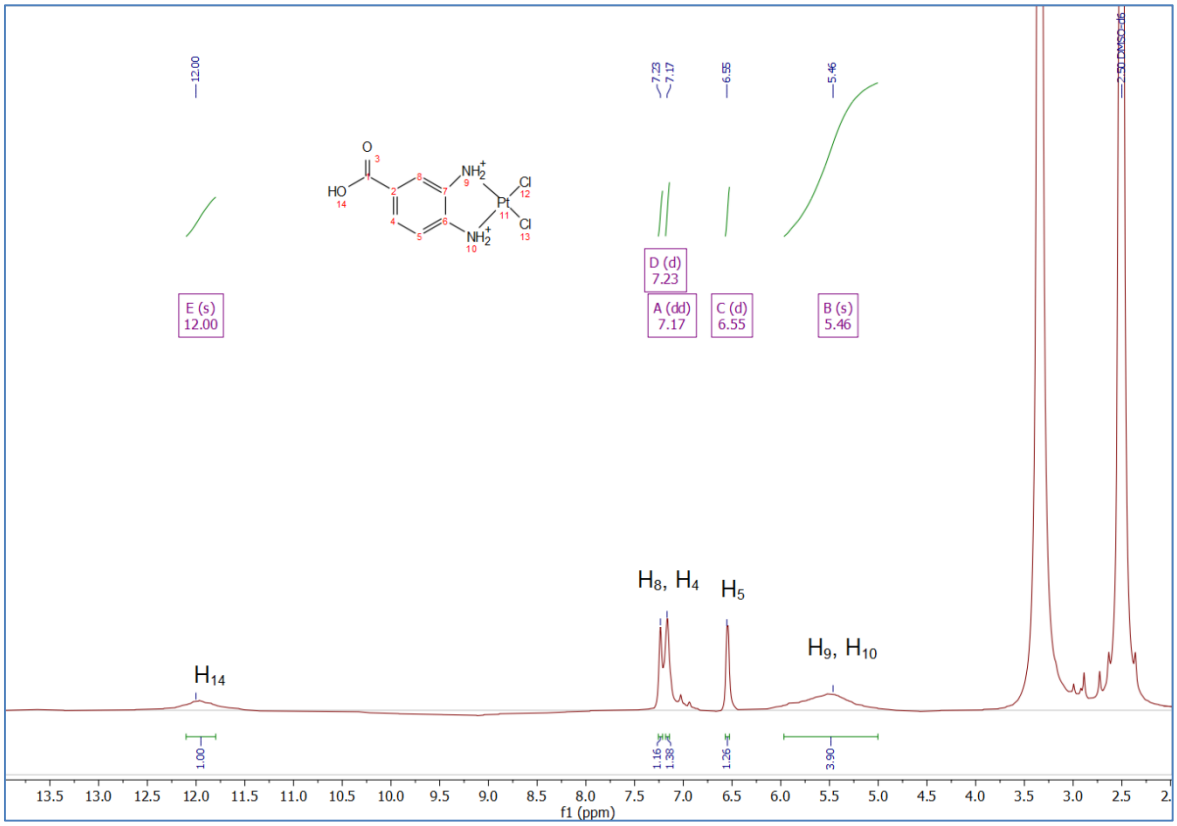

Figure S7. ^{1}H NMR spectra of **[Pt(II)(DABA)Cl$_2$]** recorded in DMSO-d$_6$ using Bruker Avance 400 (400 MHz)

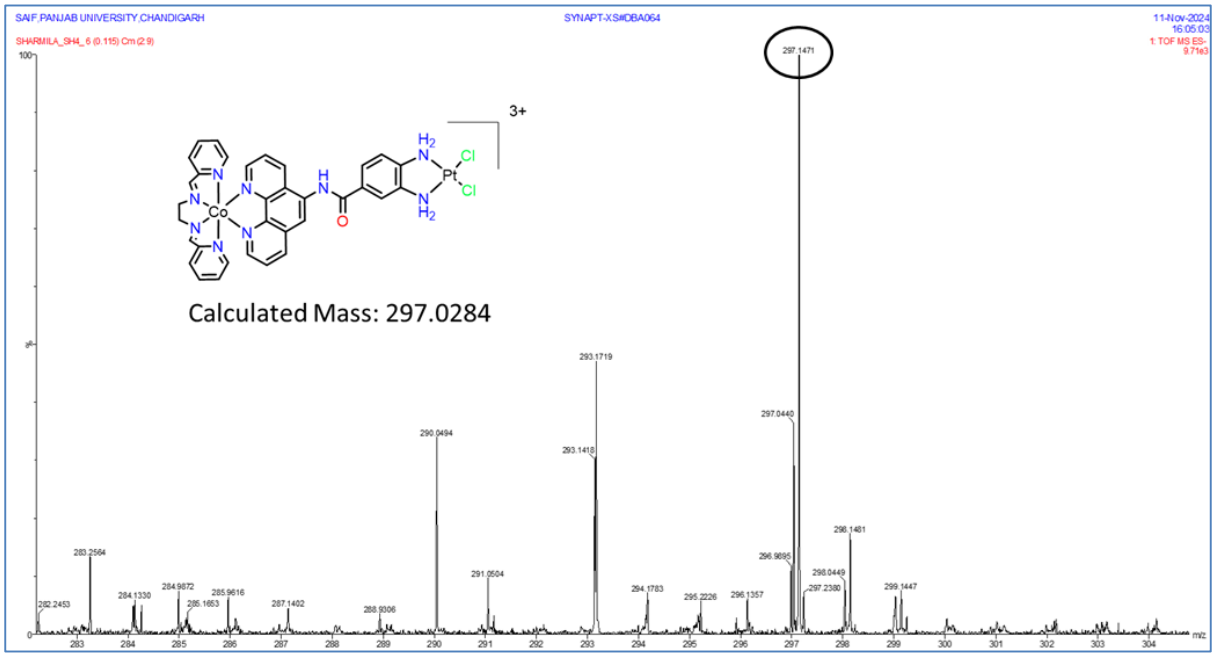

Figure S8. Q-TOF ESI Mass spectra of **[Co(III)-Pt(II)](acac)$_3$** recorded in CH$_3$OH using Waters Micromass Q-Tof Micro spectro-photometer. The peak at m/z 297.1471 corresponds to the species [M]$^{3+}$ of complex **[Co(III)-Pt(II)](acac)$_3$**

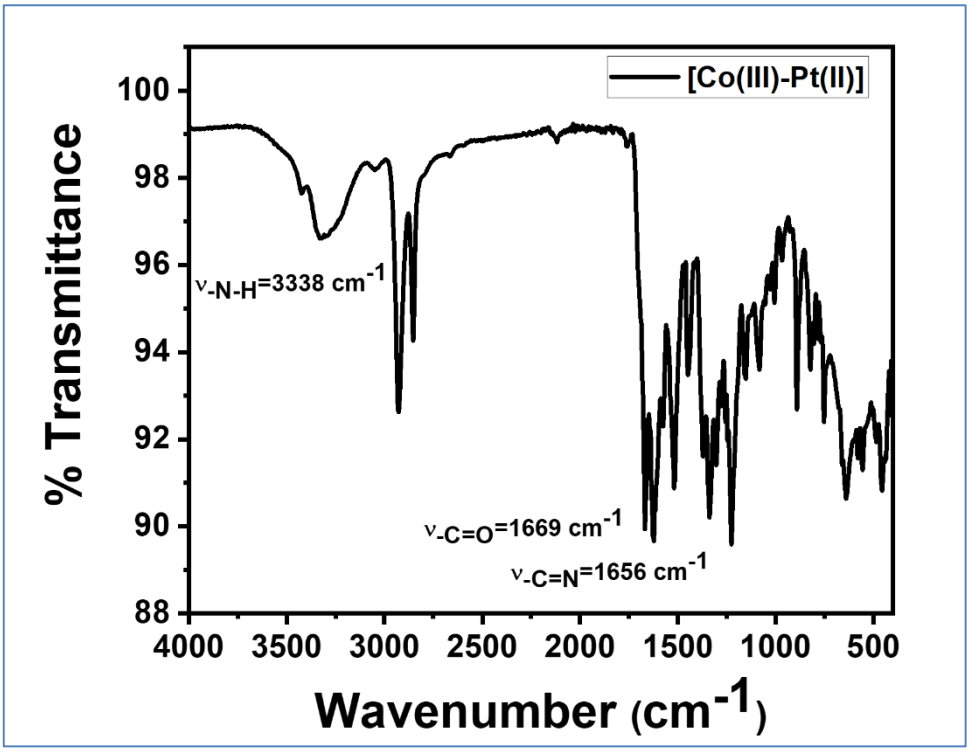

Figure S9. FT-IR Spectra of **[Co(III)-Pt(II)](acac)$_3$** with characteristics peaks at 1656 cm^{-1} ,1669 cm^{-1} and 3338 cm^{-1} representing imine bond, carbonyl bond and amine bond recorded using Perkin-Elmer UATR TWO FT-IR Spectrometer

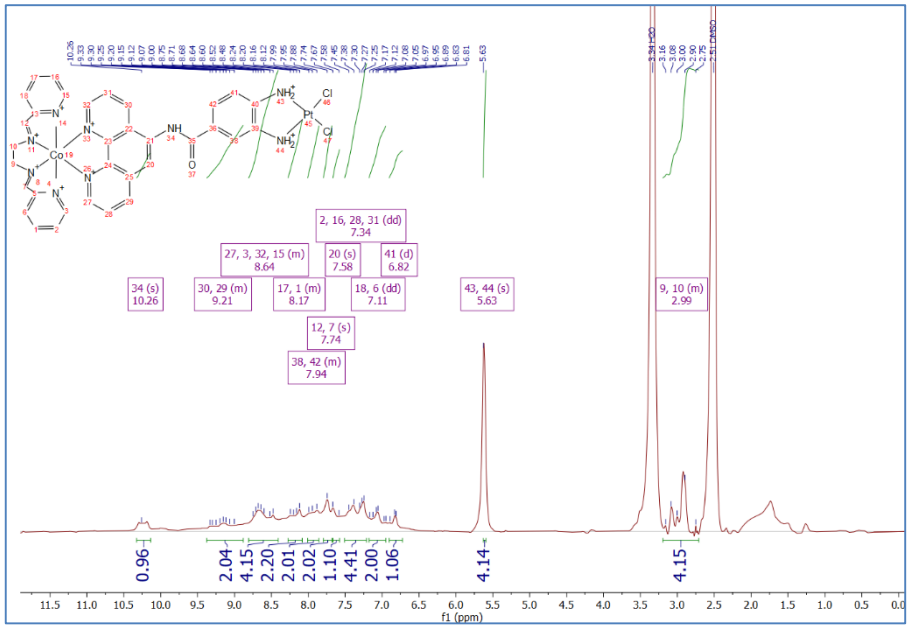

Figure S10. ^{1}H NMR spectra of **[Co(III)-Pt(II)](acac)$_3$** recorded in DMSO-d$_6$ using Bruker Avance 400 (400 MHz). The signals in the aromatic region between δ 9.2-6.82 ppm correspond to the protons of the coordinated 1,10-phenanthroline, the Schiff base and the DABA ligand. The most downfield signal at δ 10.26 ppm (s) is assigned to the NH proton of the amide bond. The singlet at δ 5.63 ppm corresponds to the amino (–NH$_2$) protons of the pendant aromatic amine group. The peaks at δ 2.96-2.67 are attributed to aliphatic CH$_2$ protons of the ancillary ligand. In the ^{1}H NMR spectra of diamagnetic metal–acetylacetonate complexes, the acac ligand is typically characterised by two well-

defined resonances: a singlet for the methine proton (–CH–) at δ 5.3–5.5 ppm and a singlet for the two equivalent methyl substituents at δ 1.8–2.0 ppm, as observed for $Co(acac)_3$ in solution. (Ref. G. M. Shalhoub, *J. Chem. Educ.,* 1980, **57**, 525) In contrast, when acetylacetonate is present as a counter-ion, the expected signals usually appear in the same spectral region, but they are frequently broadened or coalesced due to ion pairing and dynamic exchange processes. Such behaviour in the case of $Co(cyclam)(acac)_2$, noting that the acetylacetonate counter-ion resonances were detected but overlapped and insufficiently resolved for precise chemical-shift assignment (Ref. E. Simon, P. L'Haridon, R. Pichon and M. L'Her, *Inorg. Chim. Acta*, 1998, **282**, 173–179).

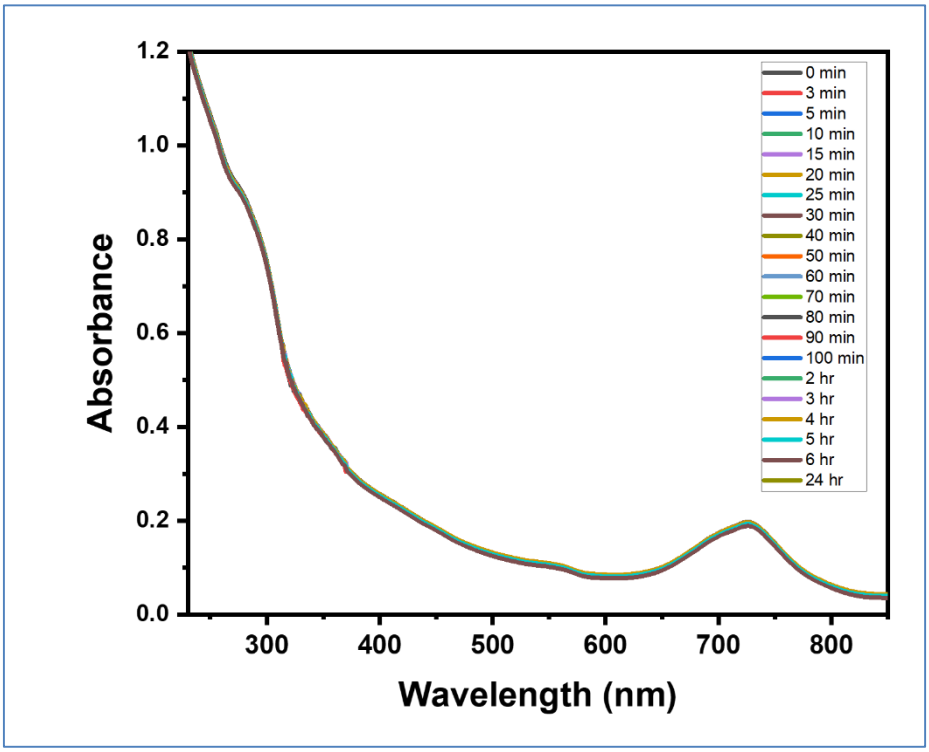

Figure S11. Stability study of **$[Co(III)\text{-}Pt(II)](acac)_3$** (1 $mmol.L^{-1}$) in 2% DMSO/PBS buffer at pH 7.4 by UV-visible spectroscopy.

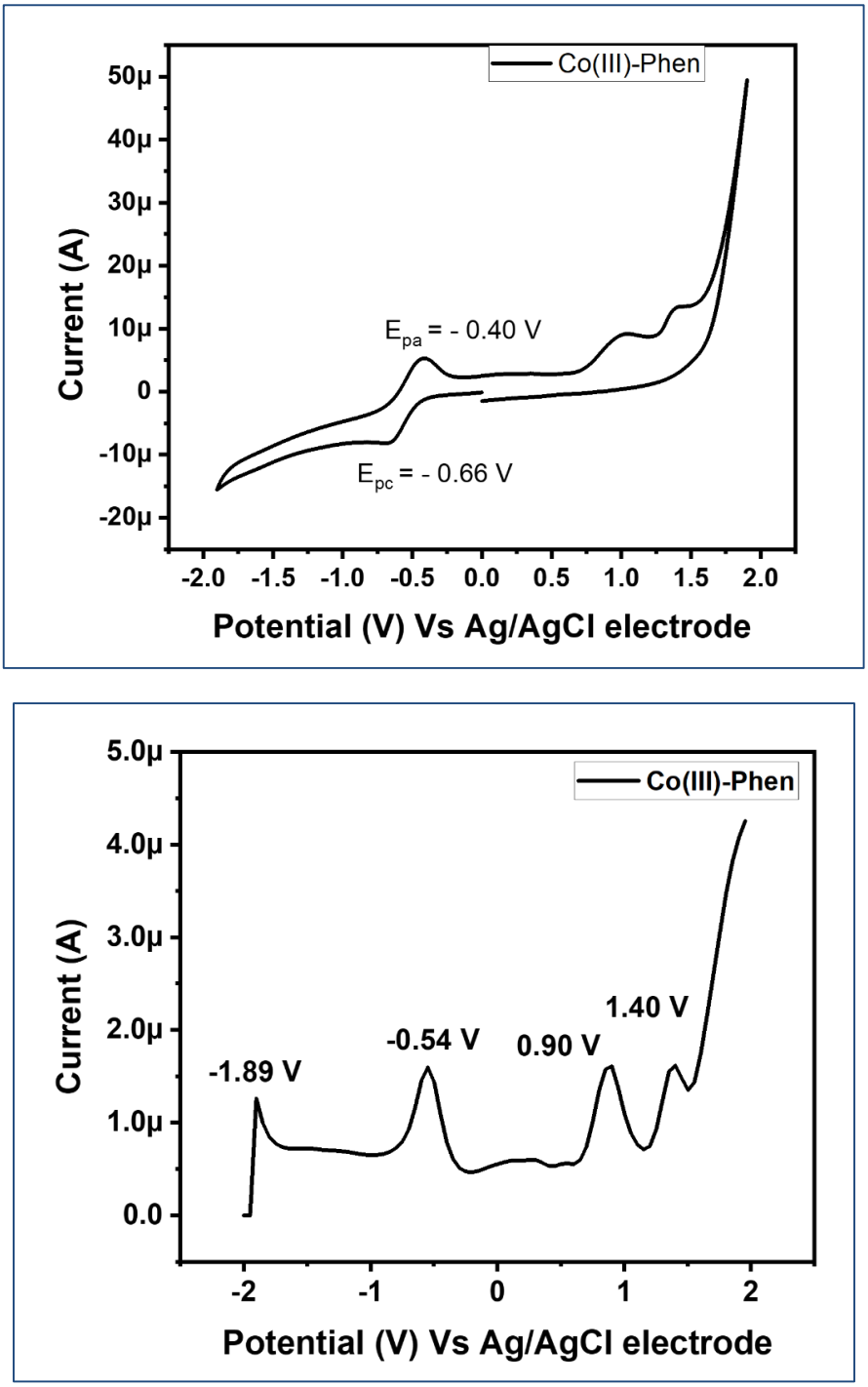

Figure S12. Cyclic Voltammogram and Differential Pulse Voltammogram of **[Co(III)(L^1)(phen-NH_2)](acac)$_3$** using solution (20 mL (1mM)) in 2% DMSO-PBS buffer at 298 K using Glassy Carbon electrode as working electrode, Ag/AgCl electrode as reference electrode and Pt electrode as counter electrode and KCl 0.1 M as supporting electrolyte, at scan rate 50 mV/s.

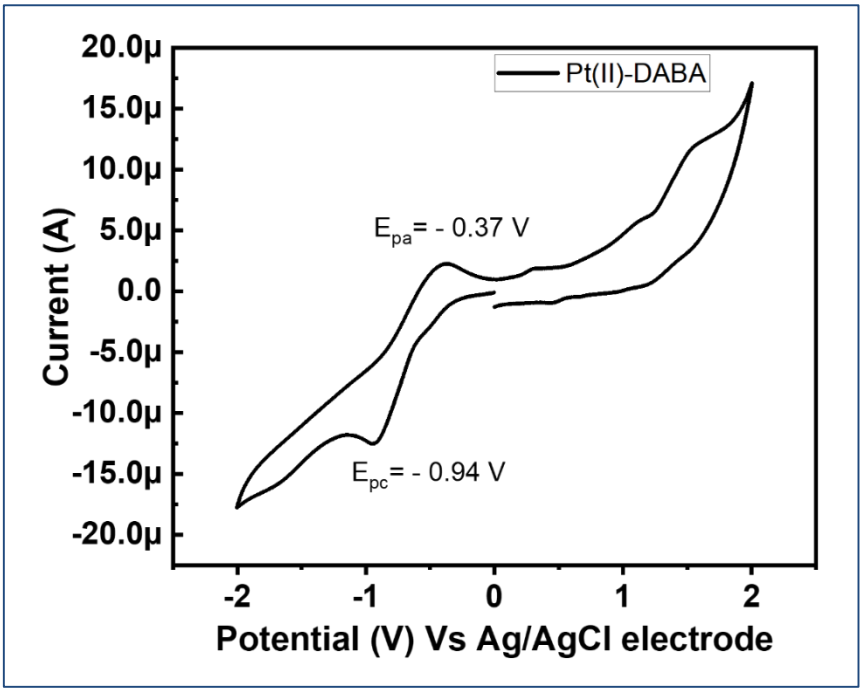

Figure S13. Cyclic Voltammogram of **[Pt(II)(DABA)Cl_2]** using solution (20 mL (1mM)) in 2% DMSO-PBS buffer at 298 K using Glassy Carbon electrode as working electrode, Ag/AgCl electrode as reference electrode and Pt electrode as counter electrode and KCl 0.1 M as supporting electrolyte, at scan rate 50 mV/s.

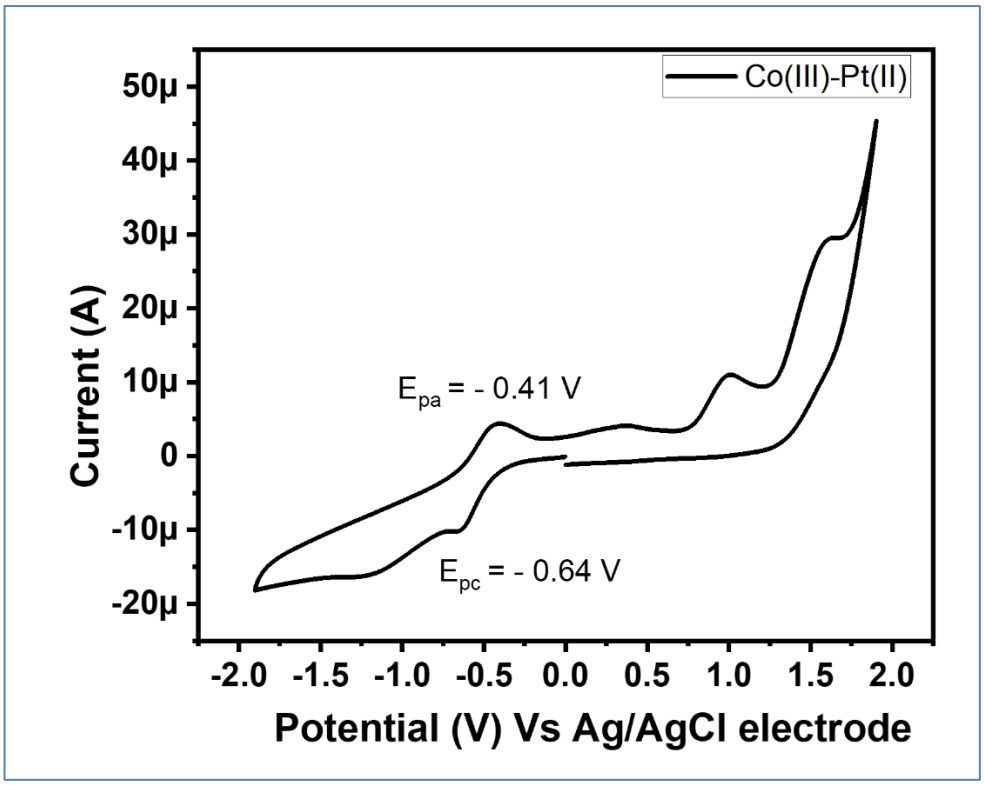

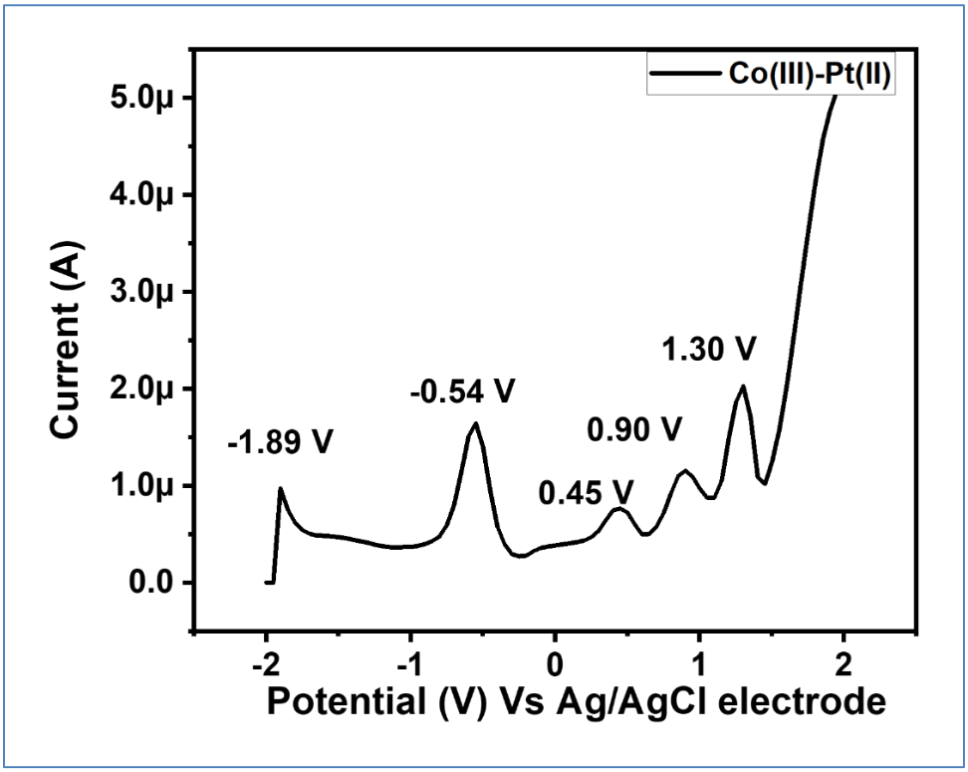

Figure S14. Cyclic Voltammogram and Differential Pulse Voltammogram of **[Co(III)-Pt(II)](acac)$_3$** using solution (20 mL (1mM)) in 2% DMSO-PBS buffer at 298 K using Glassy Carbon electrode as working electrode, Ag/AgCl electrode as reference electrode and Pt electrode as counter electrode and KCl 0.1 M as supporting electrolyte, at scan rate 50 mV/s.

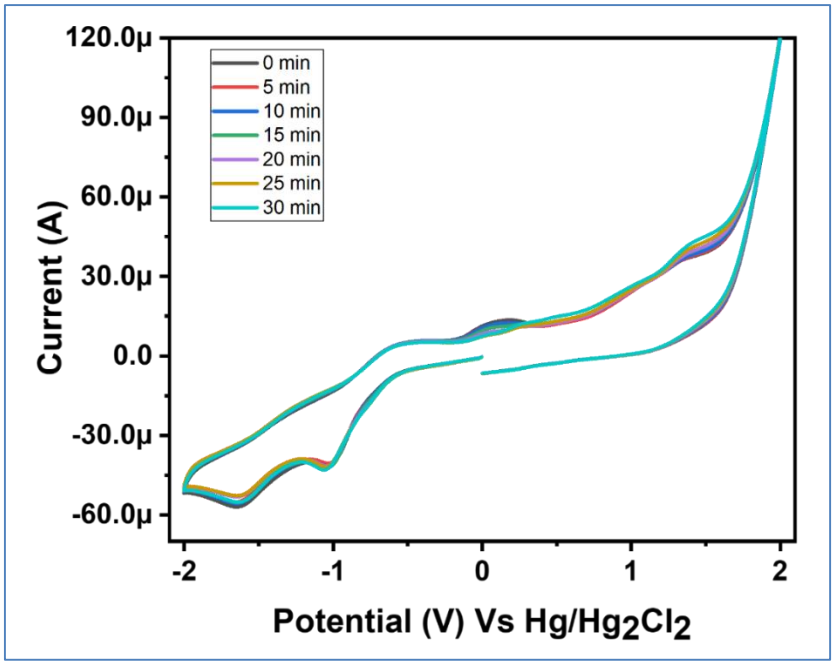

Figure S15. Stability study of **[Co(III)-Pt(II)](acac)$_3$** in Cyclic Voltammogram for 30 min using solution (20 mL (1mM)) in 2% DMSO-PBS buffer at 298 K using Glassy Carbon electrode as working electrode, Hg/Hg_2Cl_2 electrode as reference electrode and Pt electrode as counter electrode and KCl 0.1 M as supporting electrolyte, at scan rate 0.5 V/s.

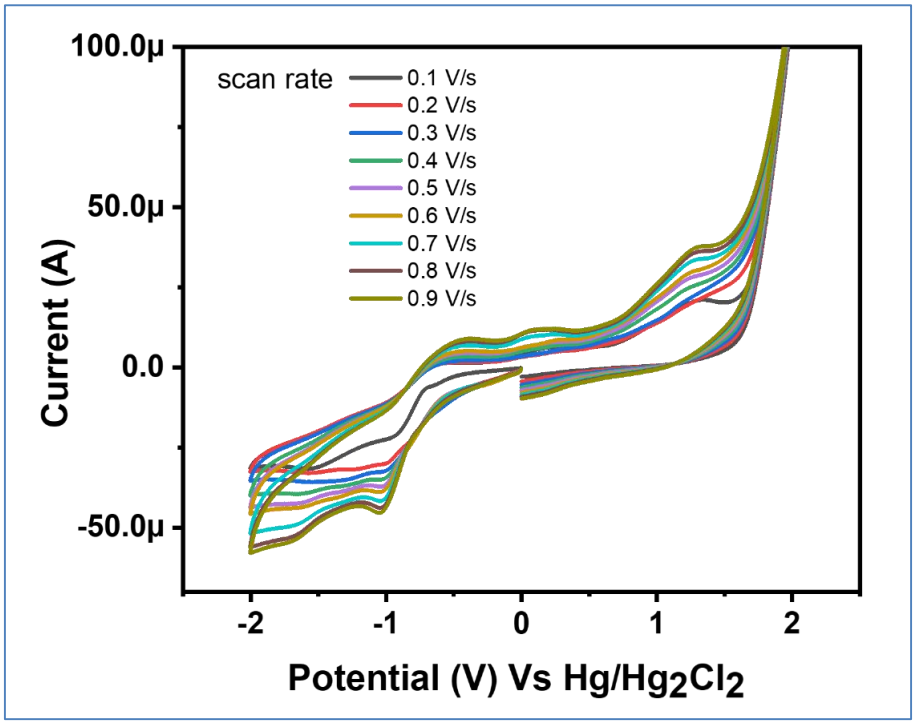

Figure S16. Study of electrochemical behaviour of **[Co(III)-Pt(II)](acac)$_3$** in Cyclic Voltammogram at different scan rate using solution (20 mL (1mM)) in 2% DMSO-PBS buffer at 298 K using Glassy Carbon electrode as working electrode, Hg/Hg_2Cl_2 electrode as reference electrode and Pt electrode as counter electrode and KCl 0.1 M as supporting electrolyte.

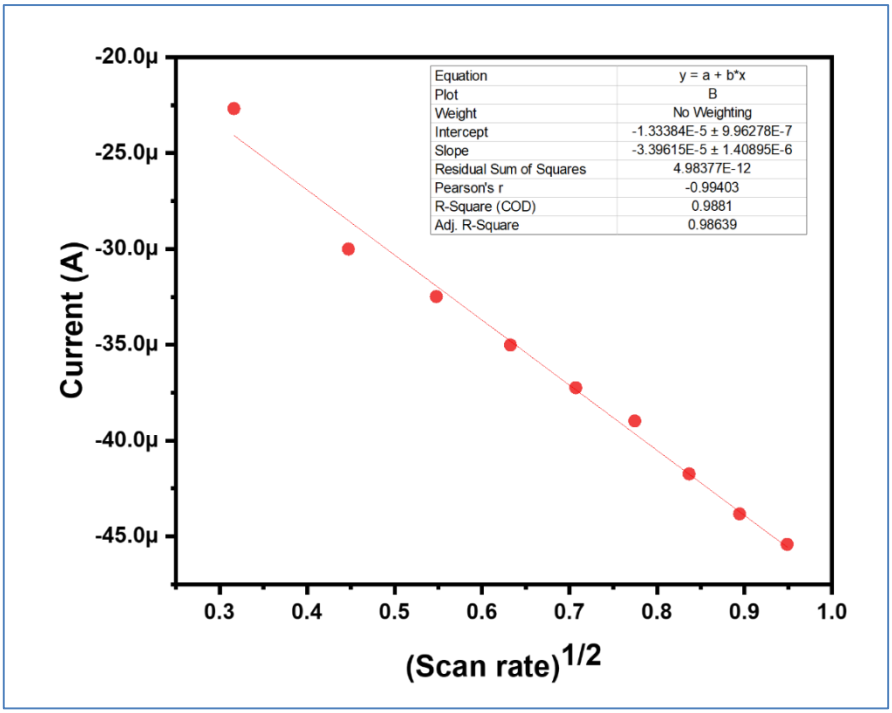

Figure S17. A linear relationship between the cathodic peak current (I_p) and the square root of the scan rate ($v^{1/2}$) indicates diffusion-controlled electron transfer. Fitting was performed using linear regression.

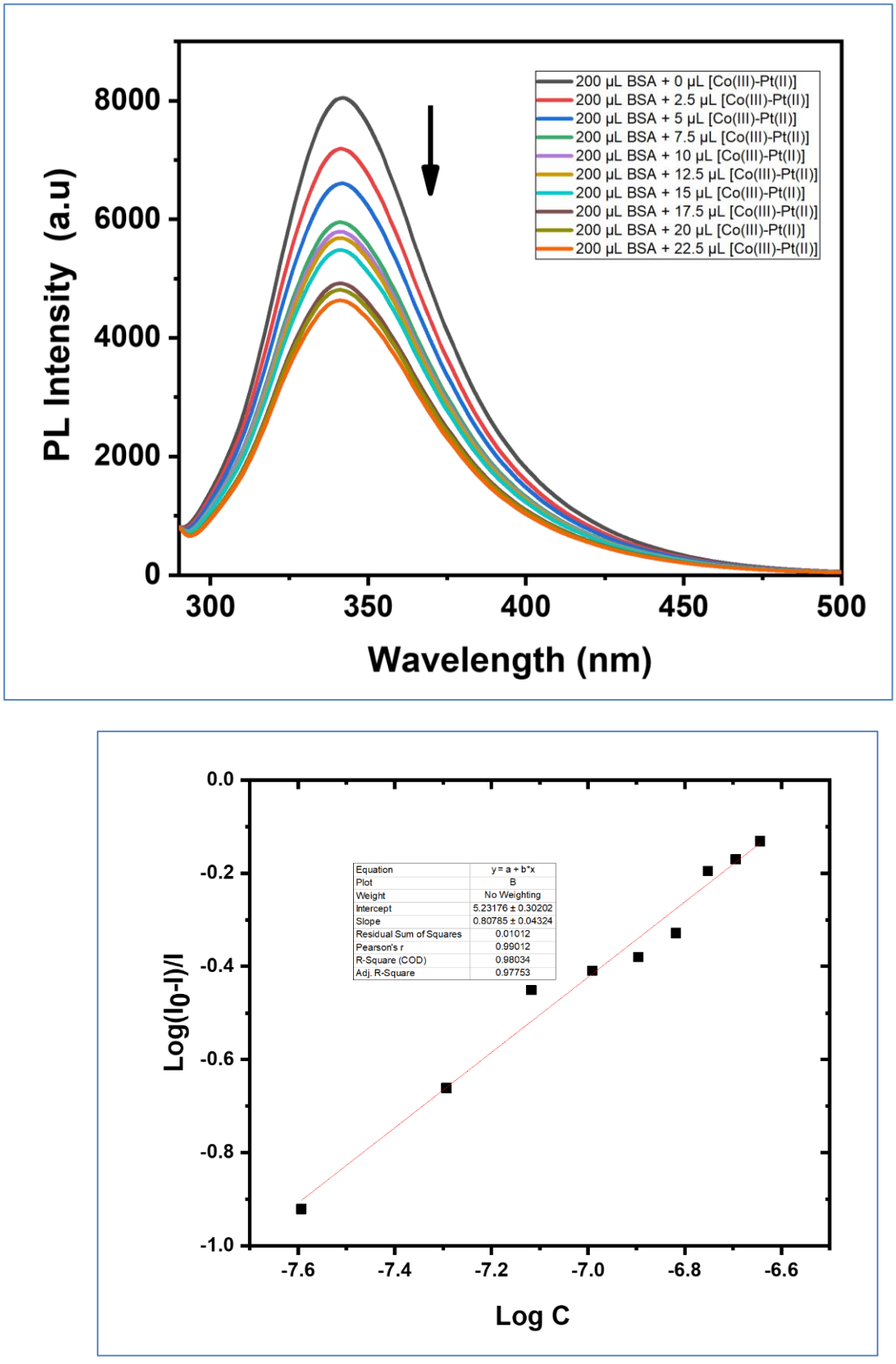

Figure S18. Photoluminescence plot and Scatchard plot of **[Co(III)-Pt(II)](acac)$_3$** for BSA binding.

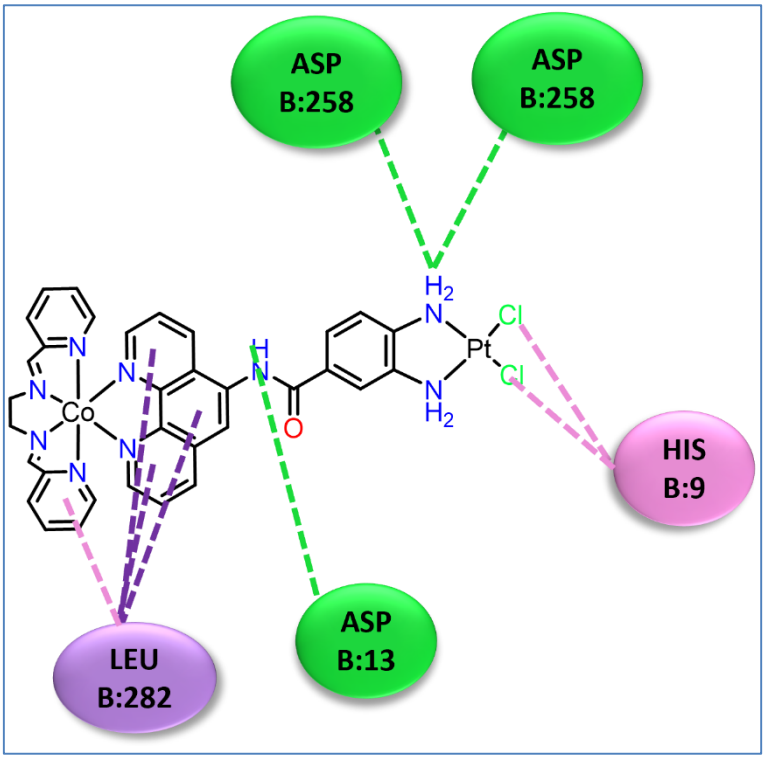

Figure S19. Molecular Docking interaction map of **[Co(III)-Pt(II)](acac)$_3$** with BSA

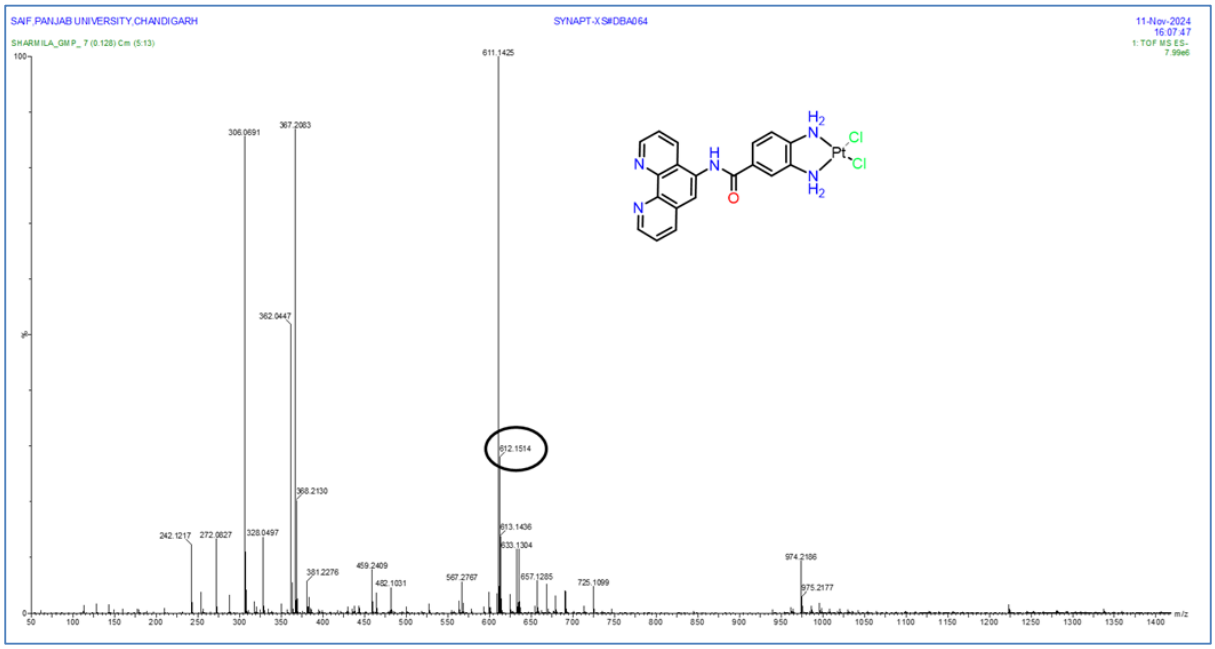

Figure S20. Q-TOF ESI Mass spectra recorded for the methanolic solution of [Co(III)-Pt(II)] and GSH (10 mM) using Waters Micromass Q-Tof Micro spectro-photometer. The peak at m/z 612.1514 corresponds to $[Pt(II)+NH_4]^+$ moiety released after reduction of Co(III) to Co(II).

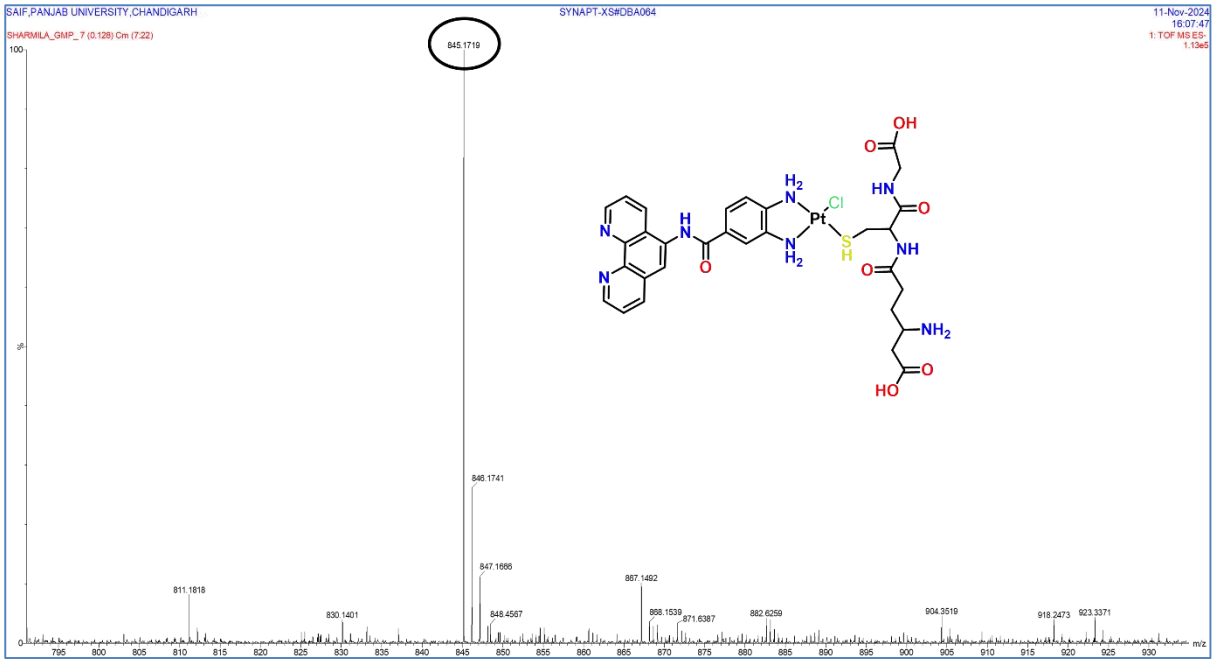

Figure S21. Q-TOF ESI Mass spectra of complex-GSH adduct recorded for the methanolic solution of [Co(III)-Pt(II)] and GSH (10 mM) using Waters Micromass Q-Tof Micro spectro-photometer. The peak at 845.1719 m/z corresponds to [PtGSH-Cl-H], confirming the coordination of GSH in the Pt centre.

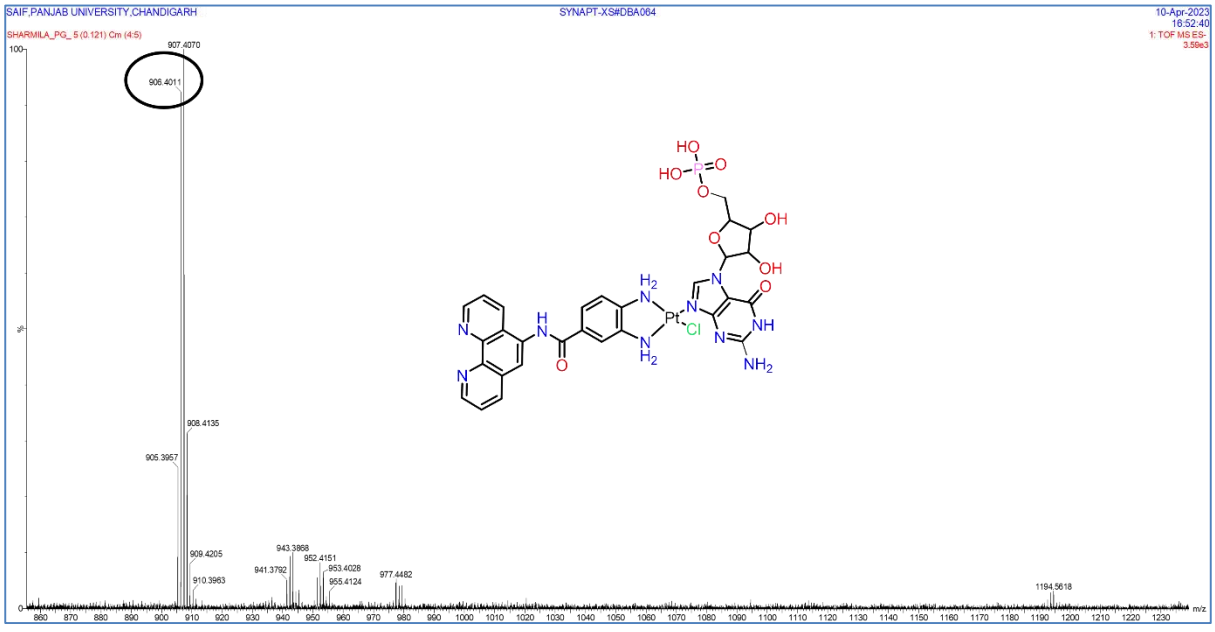

Figure S22. Q-TOF ESI Mass spectra of complex-GMP adduct recorded for the methanolic solution of [Co(III)-Pt(II)], GSH (10 mM), and GMP using Waters Micromass Q-Tof Micro spectro-photometer. The peak at m/z 906.4011 corresponds to $[PtGMP\text{-}OH]^+$ adduct, confirming the coordination of GMP to the platinum centre after reduction-induced Pt release.

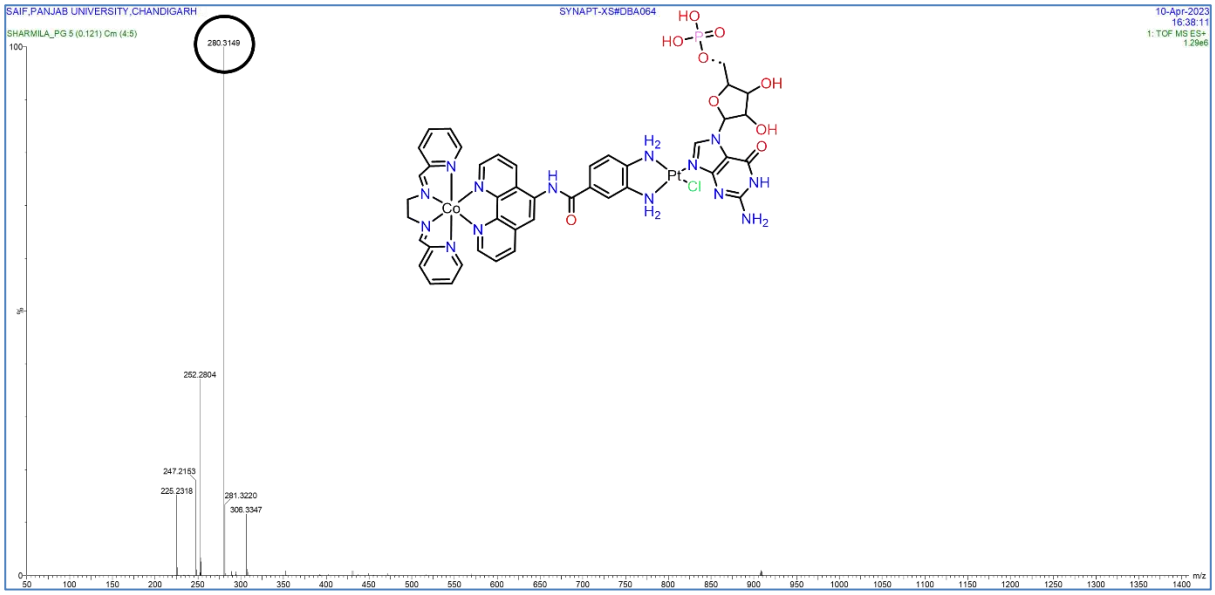

Figure S23. Q-TOF ESI Mass spectra of complex-GMP adduct recorded for the methanolic solution of [Co(III)-Pt(II)] and GMP using Waters Micromass Q-Tof Micro spectro-photometer. The peak at m/z 280.3149 corresponds to the tetracationic species $[M–PO_4H_2]^{4+}$, consistent with coordination of GMP to the platinum center.

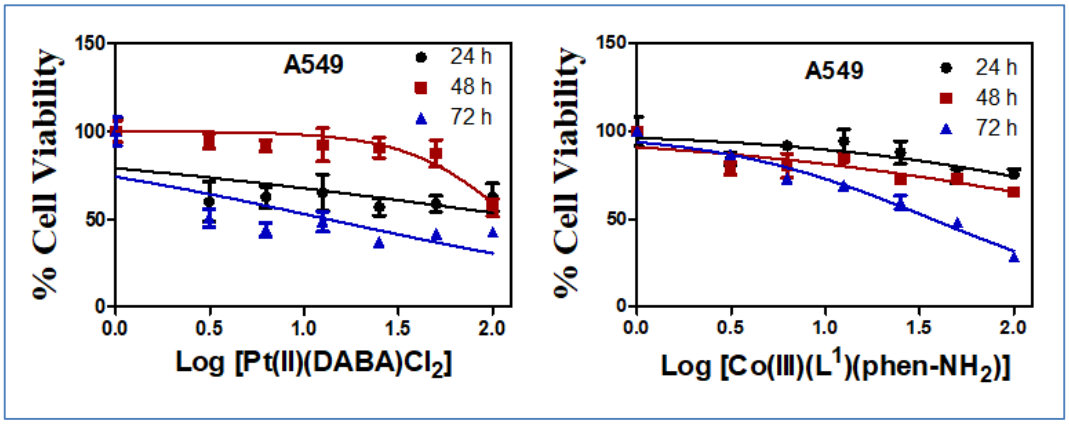

Figure S24. Non-linear regression plot for cellular viability data in A549 cells for **[Pt(II)(DABA)Cl$_2$]** and **[Co(III)(L^1)(phen-NH$_2$)](acac)$_3$** using GraphPad Prism 5 for a period of 24h, 48 h and 72 h. Both complexes exhibit significant reductions in cell viability with increasing concentrations. Data are expressed as mean ± standard deviation.

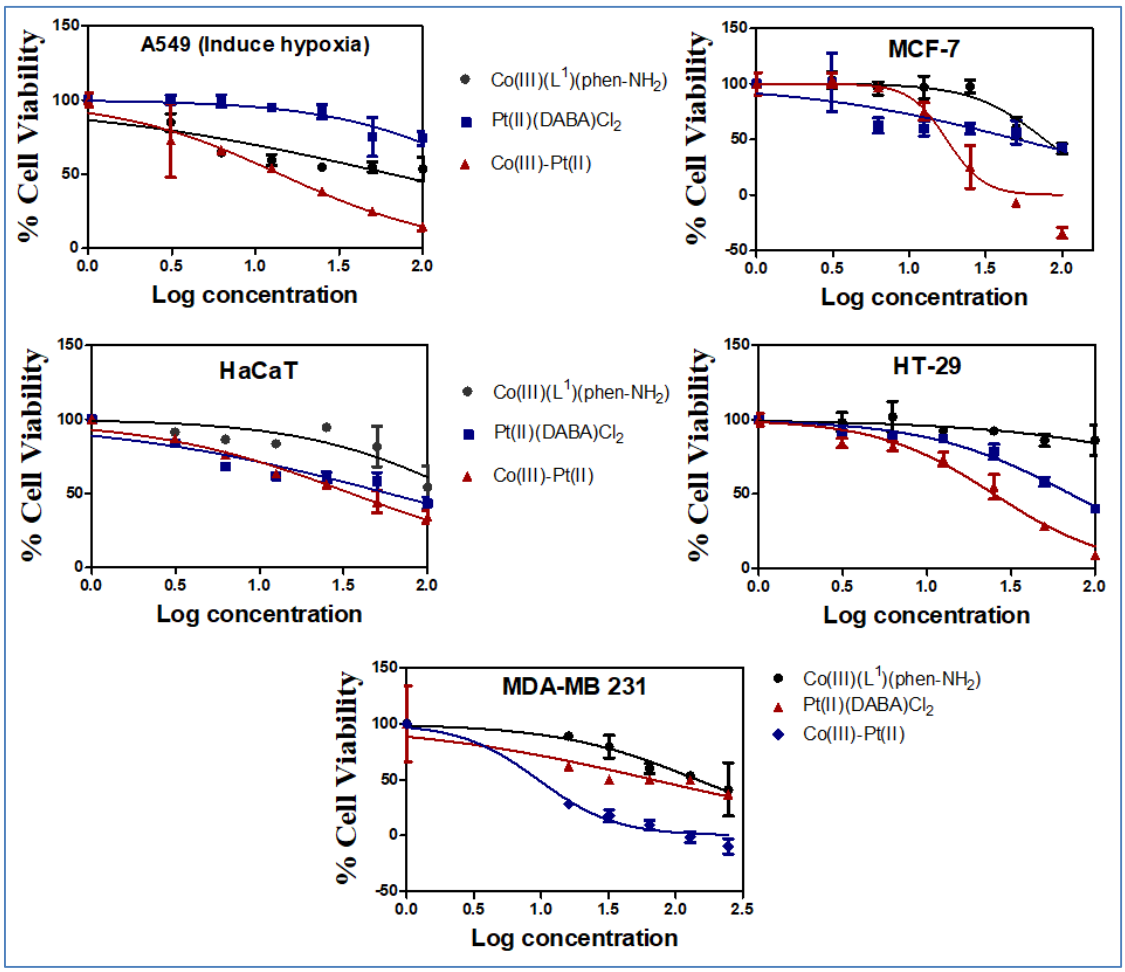

Figure S25. Non-linear regression plot for cellular viability data in A549 (hypoxia), MCF-7, HaCaT, HT-29, and MDA-MB-231 cells using GraphPad Prism 5. Data are expressed as mean ± standard deviation.

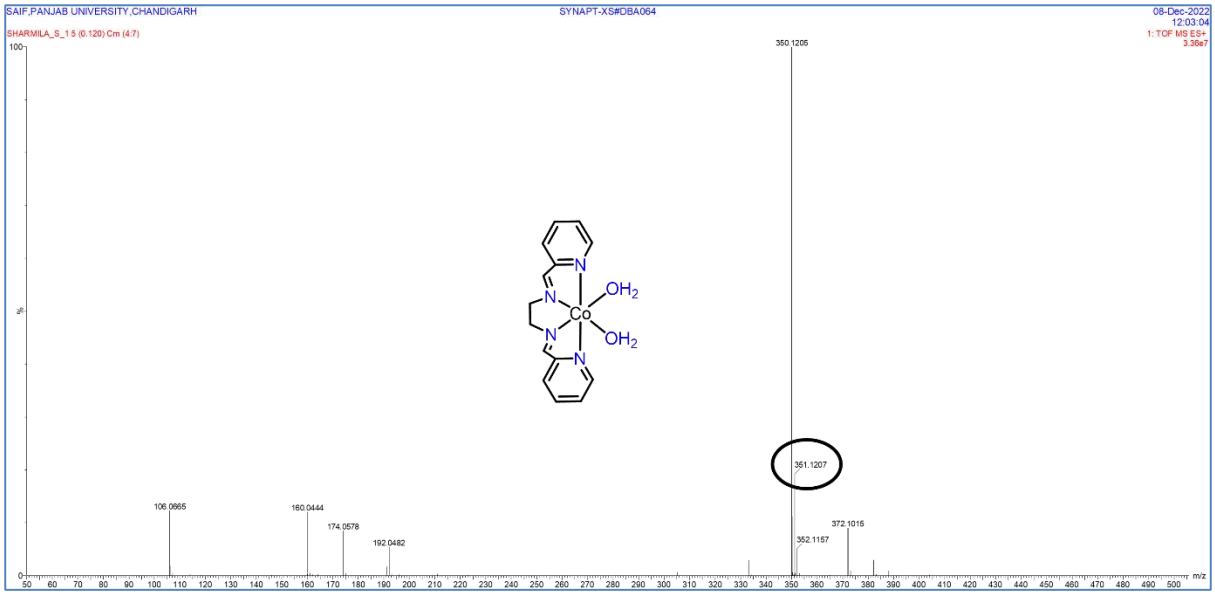

Figure S26. Q-TOF ESI Mass spectra recorded for the methanolic solution after the treatment of the [Co(III)–Pt(II)] complex with GSH using Waters Micromass Q-Tof Micro spectro-photometer. The peak at m/z 351.1207 is assigned to $[Co(II)L^1(H_2O)_2]$, indicating reduction of Co(III) and release of the Pt(II) moiety

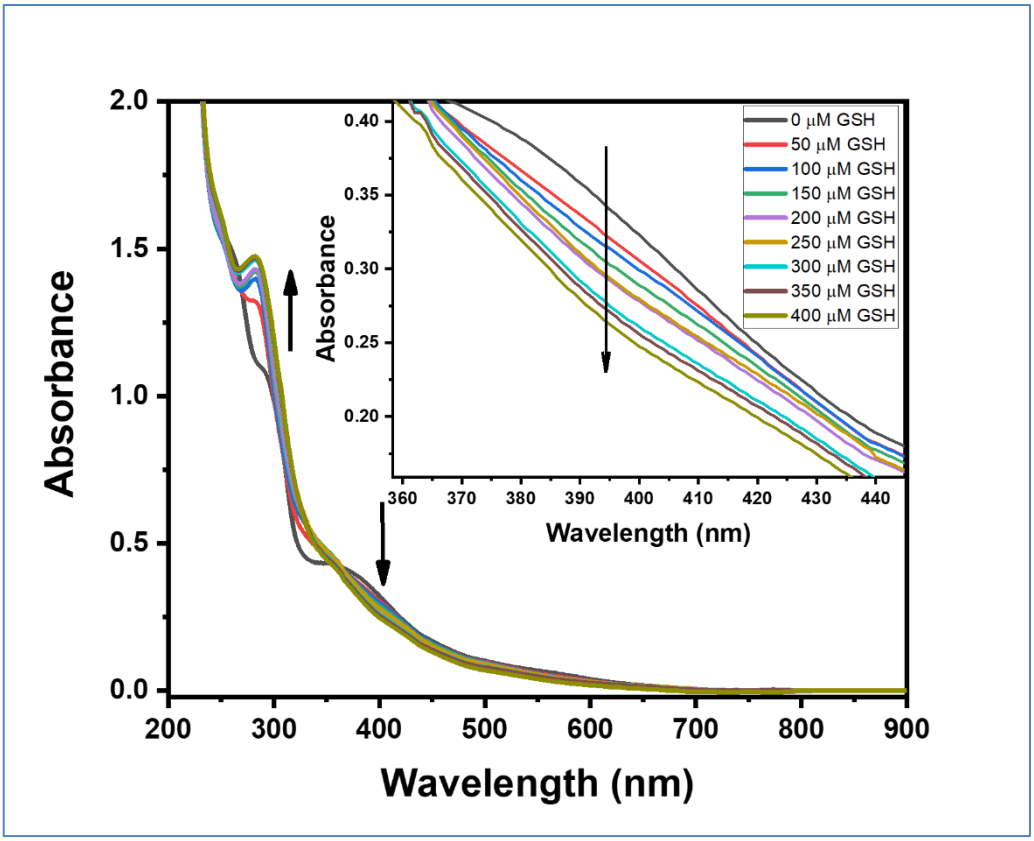

Figure S27. UV–Vis spectra of $Co(III)L^1(phen\text{-}NH_2)$ (80μM) (recorded upon addition of GSH (50–400 μM). There is a decrease in the LMCT band in the 350-400 nm region, indicating a possible reduction of Co(III) to Co(II). The increase in the 280-290 nm region is attributed to ligand-centered π-π* transition of phenanthroline, suggesting partial ligand dissociation.

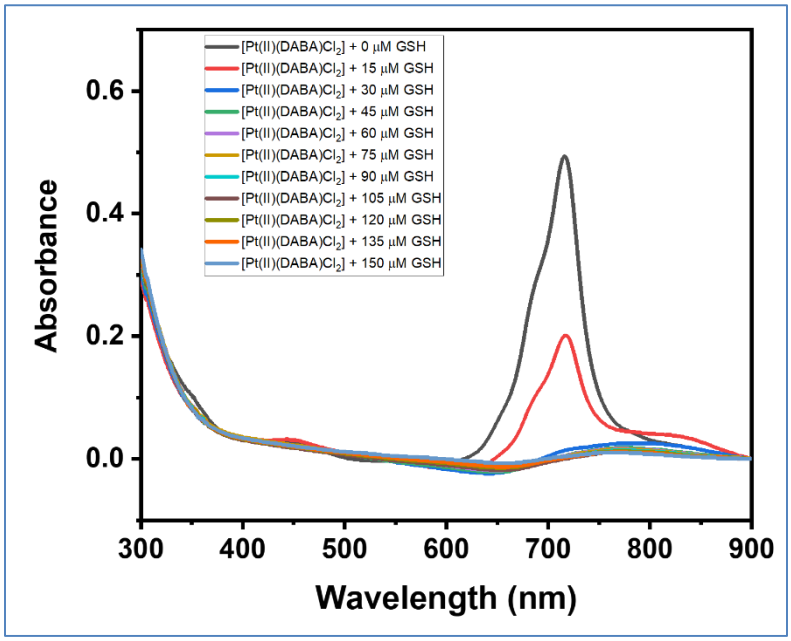

Figure S28. UV–Vis spectral changes of [Pt(II)(DABA)Cl_2] (20 µM) upon step-wise addition of GSH (15-150 µM). The progressive decrease in the 650–750 nm band indicates the reduction/substitution of the original Pt complex by GSH.

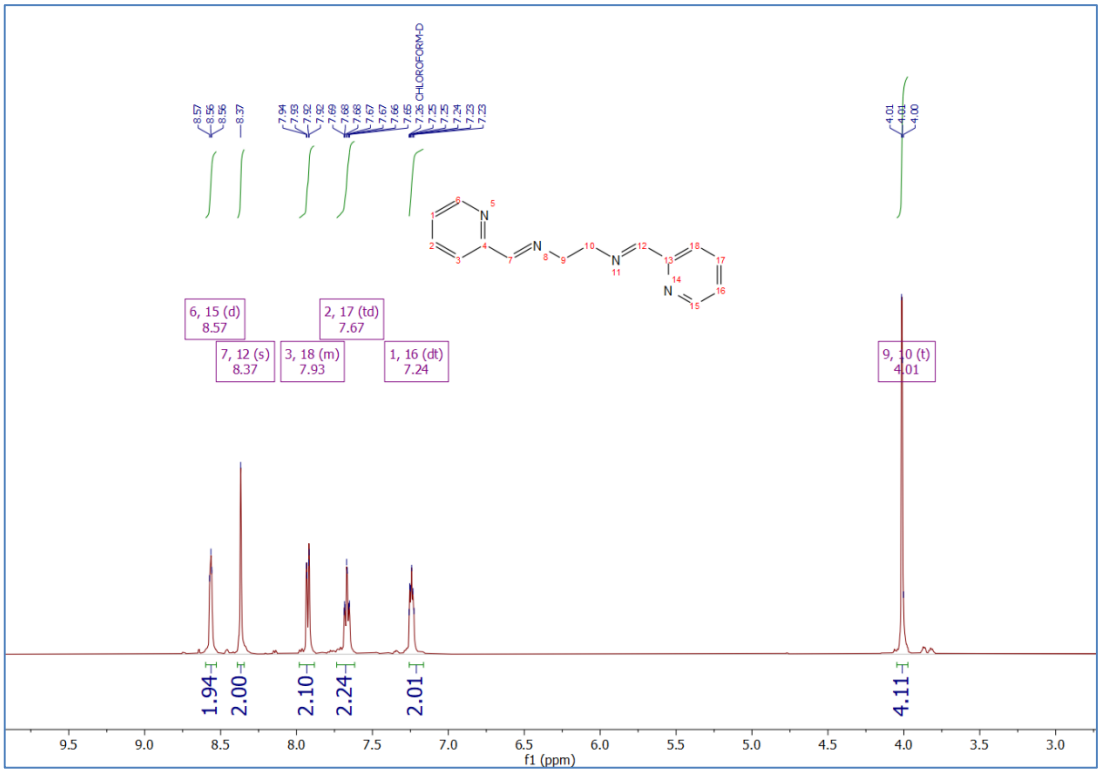

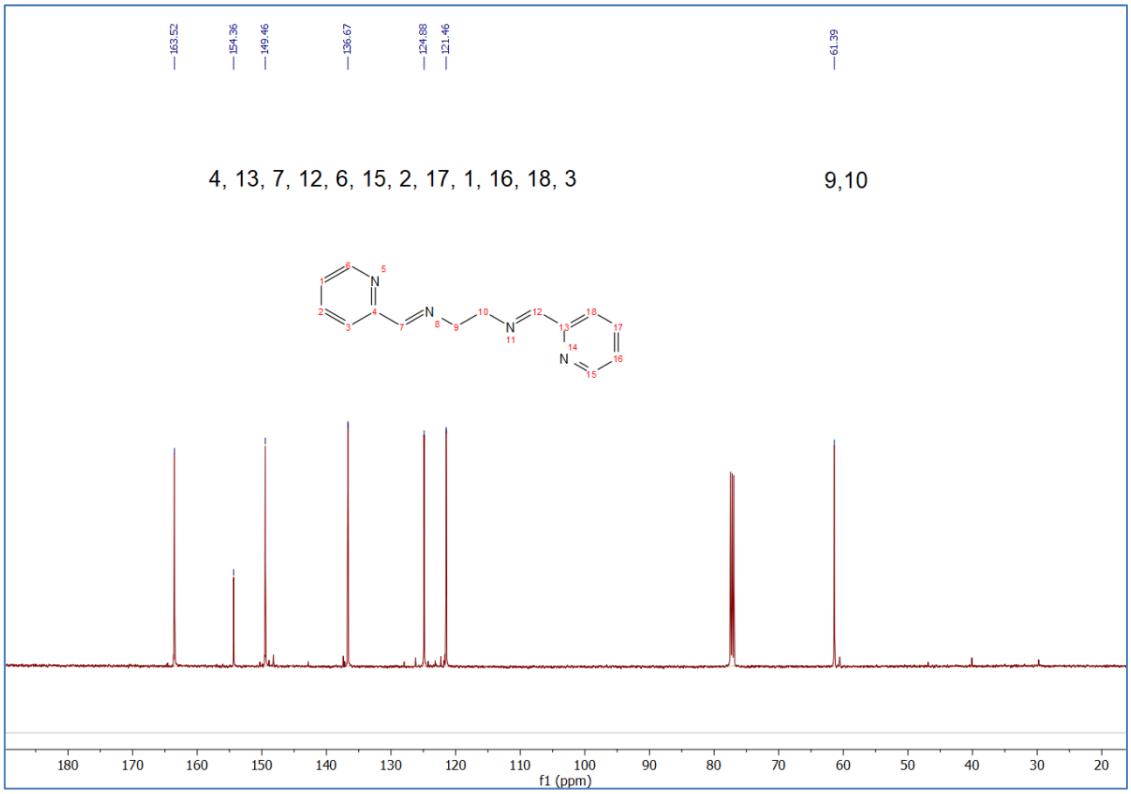

Figure S29. ^{1}H NMR and ^{13}C NMR of L_1 recorded in $CDCl_3$ using Bruker Avance 400 MHz spectrometer. The Peaks are reported to be as per the value.

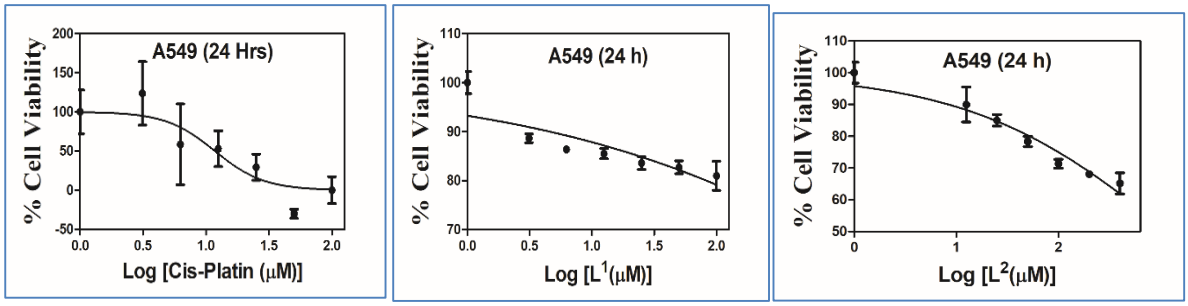

Figure S30. Non-linear regression plot for cellular viability data of Cis-Platin, L^1 and L^2 in the A549 cell line.

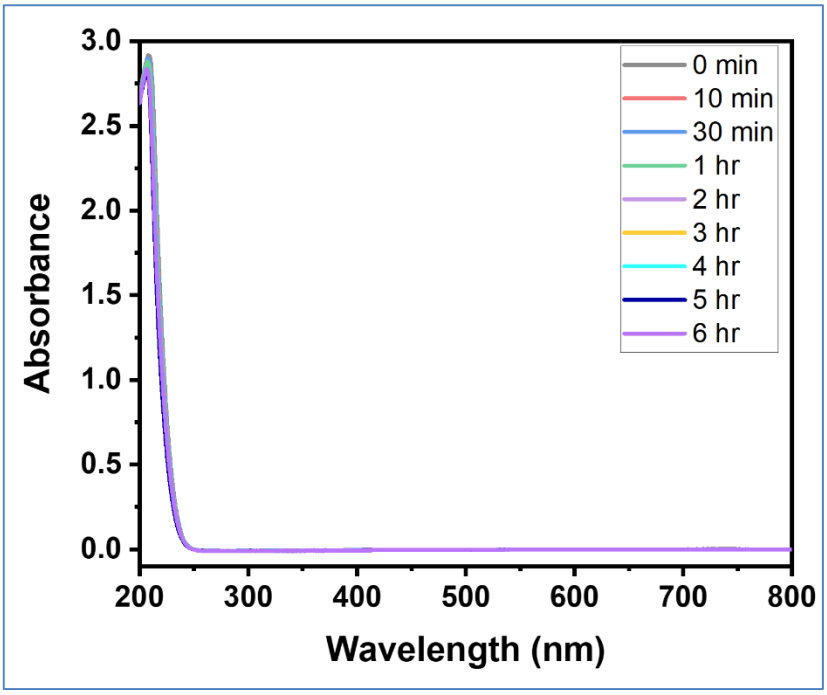

Figure S31. Time-dependent (0 to 6 hours) UV-Vis spectra of GSH (1 mM) recorded under the same experimental conditions used for the reaction with the Co-Pt complex. No changes are observed in the spectral profile over time, indicating that GSH does not undergo detectable aerial oxidation during the experimental timeframe.

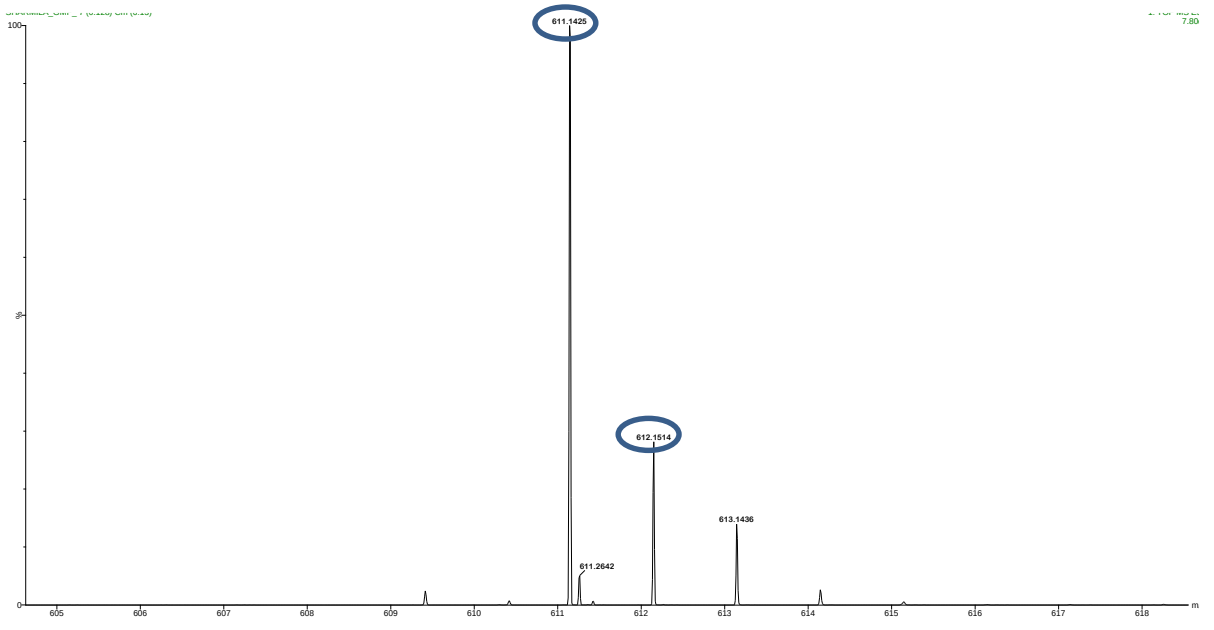

Figure S32. The isotopic distribution spectrum showing a minor peak at m/z 612.1514 corresponding to $[Pt(II)+NH_4]^+$, and a much more intense peak at m/z 611.1425 that may correspond to the isotopic pattern of the peak $[Pt(II)+NH_4]^+$.

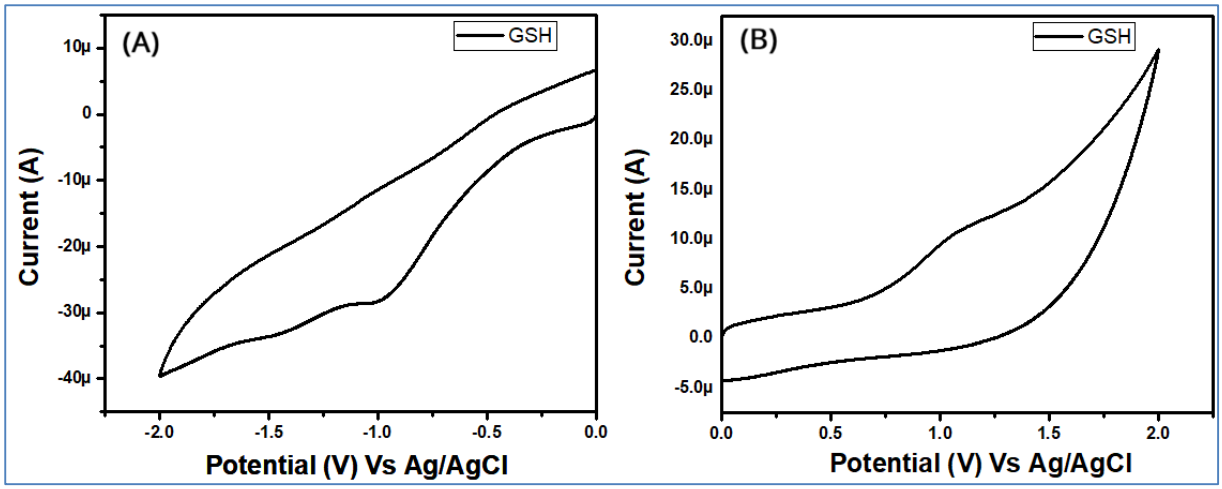

Figure S33. Cyclic Voltammogram of GSH using Ag/AgCl electrode as reference electrode A) Negative Reduction half scan; B) Positive Oxidation half scan. In the negative potential window, the GSH-only CV shows no discrete reduction peaks, as expected for GSH, which lacks reducible centers in this range. The anodic wave observed at positive potentials (+0.8 to +1.3 V vs Ag/AgCl) corresponds to GSH oxidation.

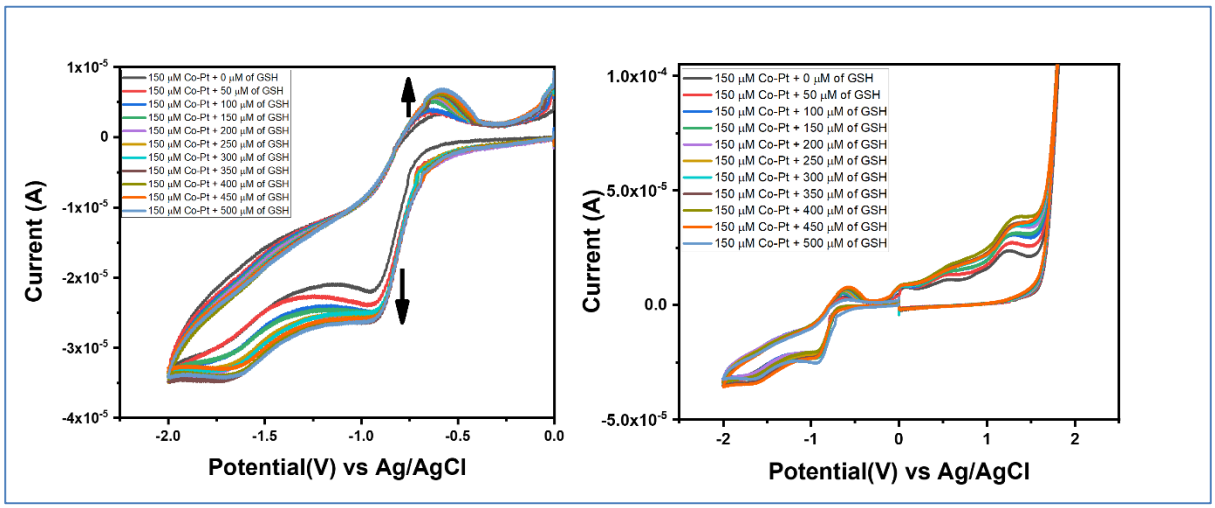

Figure S34. Cathodic and Full scan of cyclic voltammogram of Co(III)-Pt(II) complex (150µM) with increasing concentration of GSH (0- 500 µM). It reveals a pronounced enhancement in cathodic current, indicating facilitated reduction of the complex. The fact that $E_{1/2}$ shifts only marginally with increasing GSH concentration indicates that GSH does not significantly alter the thermodynamic redox potential of the metal center.

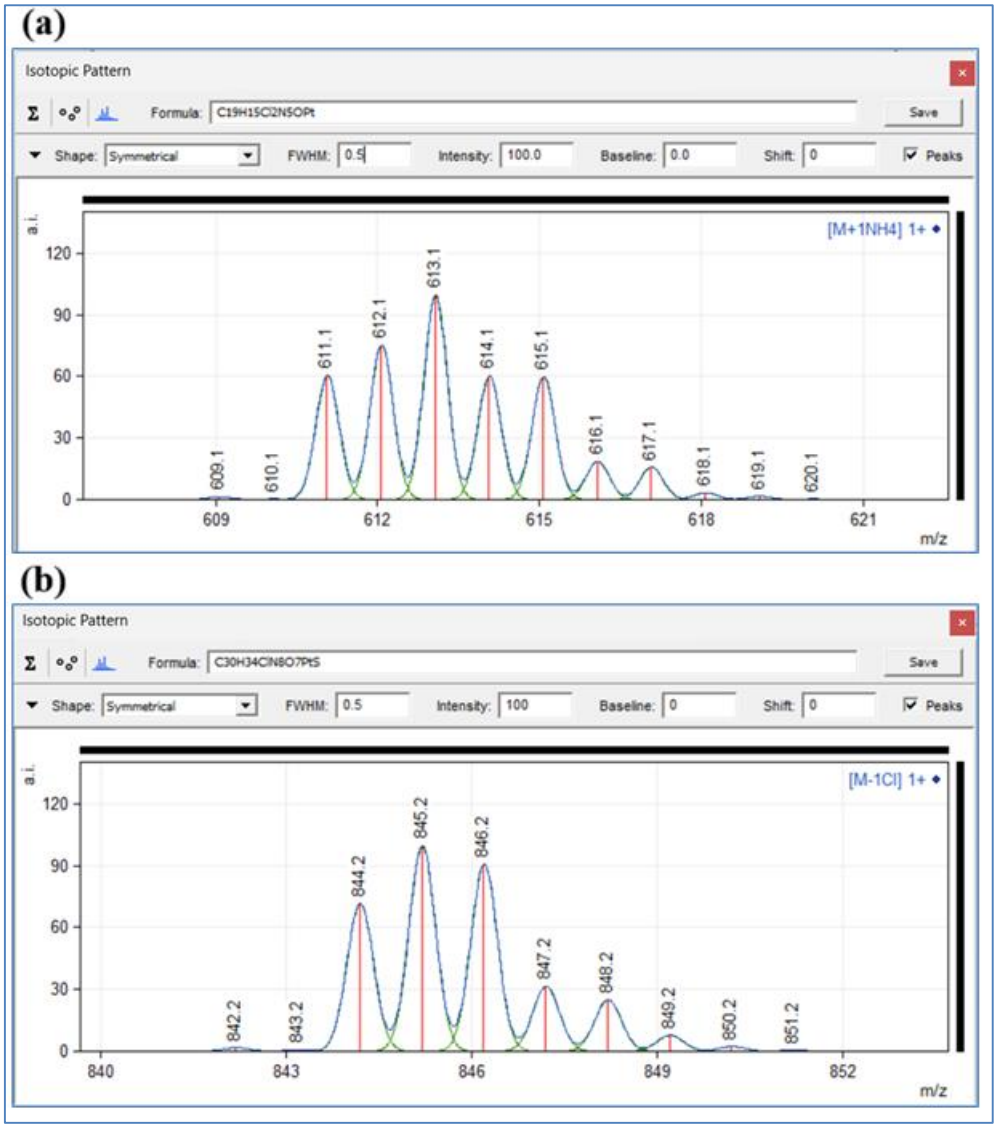

Figure S35. Simulated mass spectra showing isotropic distribution of the ion (a) $[M+NH_4]^+$, M=$[Pt(II)(C_{19}H_{15}N_5O)Cl_2]$ at 612 (b) $[M-Cl]^+$, M= $[Pt(II)(C_{19}H_{15}N_5O)(GSH)Cl]$ at 845 using mMass free software.

Reference

- **S1**. A. A. E. de Araújo Motta, M. C. S. de Castro, D. Silva and C. M. Cortez, *J. Mol. Struct.*, 2021, **1223**, 129224
- **S2**. M. G. Trachioti, A. C. Lazanas and M. I. Prodromidis, *Microchim. Acta*, 2023, **190**, 251.
- **S3**. P. S. Chen, W. T. Chiu, P. L. Hsu, S. C. Lin, I. C. Peng, C. Y. Wang and S. J. Tsai, *J. Biomed. Sci.*, 2020**, 27**, 1-19.